A microfluidics study of the triggering of underwater landslides by earthquakes *

M. El Bettah[1,2], *S.T. Grilli*[1], *C.D.P. Baxter*[1], *K. Bollinger*[1], *M. Krafczyk*[2] *and C. Janßen*[2]

1. Department of Ocean Engineering, University of Rhode Island (URI), Narragansett, RI, USA

2. Institute for Computational Modeling in Civil Engineering, Technical University of Braunschweig (TUB), Braunschweig, Germany

ABSTRACT

Underwater landslides may be triggerred by the reduction in soil strength (sometimes up to the point of liquefaction) caused by excess inter-granular pore pressures resulting from sesimic activity. Here, we study micro-mechanical processes responsible for such excess pore pressure build up in soils, by way of microfluidics technologies, with the long term goal of contributing to the prediction of tsunamigenic landslides. Thus, both large- and small-scale experiments are performed; the former are standard cyclic triaxial tests, using both natural and idealized saturated soils, while the latter take place in custom-fabricated mini-channels, filled with water or with a mixture of water and idealized sediments. In parallel, a new Computational Fluid Dynamics model is developed based on the lattice-Boltzmann method (for the fluid phase), coupled with a "physics engine" (for the solid/granular phase). After being validated for standard analytical solutions for steady flows, the model is used to simulate the behavior of an ideal saturated granular soil, represented by rigid spheres. In future work, once it is made both more general and efficient, the model will be used to simulate mini-channel experiments, such as reported here, as well as cyclic triaxial tests.

KEYWORDS : Microfluidics technology; Lattice-Boltzmann Method; Pore pressure; Soil liquefaction; Underwater landslide.

INTRODUCTION

Although "co-seismic" tsunamis generated by earthquakes of large magnitude ($M > 8$) may be very devastating (e.g., the 12/26/04 Indian Ocean tsunami; [18]), they are fortunately quite rare. By contrast, the more frequent average magnitude earthquakes ($M = 6.5 - 8$) may destabilize sediments on, or near, the continental shelf slope, causing underwater landslides, which may themselves create significant, or even sometimes catastrophic tsunamis for nearby coastal areas (e.g., [27]). These so-called "landslide" tsunamis are usually made of shorter and more dispersive waves (e.g., [19, 30]), which upon propagating only a few to tens of minutes, due to bathymetric focusing or wave guide effects, may concentrate their energy over narrow sections of the coastline, yielding large runup and inundation (e.g., [30, 27]). While landslide tsunami generation, propagation, and coastal impact, have been well studied, both experimentally and numerically (by this group, e.g., [8, 9, 19, 30], and others), particularly for rigid slides (i.e., cohesive sediment), the triggering of submarine landslides in less- or non-cohesive soils, by the combination of seismic loading (i.e., cyclic ground shaking) causing oscillatory excess pore pressures, resulting in a reduction in soil strength or possibly liquefaction, is still poorly understood.

In this work, we study the triggering of the instability of an underwater slope, made of porous sediment, caused by the combination of seismically induced: (a) horizontal accelerations, that may cause inertia forces exceeding the shear strength of the sediment; and (b) oscillatory excess pore pressures that may cause a reduction or a total disapearance of shear strength. Some underwater landslides may in turn be tsunamigenic, but this aspect is beyond the scope of this work. Pore pressure build-up is strongly dependent upon dynamic flow propagation in the "micro-channel" network forming the sediment matrix, a process that is poorly understood and usually represented by an ad hoc (macroscopic) constitutive law. Using such constitutive laws, Navier-Stokes solvers with multiple-fluid representation have been used to simulate underwater landslides and tsunami generaiton (e.g., [1]). The novel approach presented here combines standard large-scale modeling and experiments, with new small-scale microfluidics experiments and numerical modeling. Large-scale modeling of underwater slope failure was studied in earlier work, using a state-of-the-art continuum modeling finite difference program (FLAC^{TM}; [7]). Macroscopic laboratory experiments (cyclic triaxial tests) were also performed in earlier work, for both natural and ideal-

Accepted for ISOPE 2008 Conf. (Vancouver, Canada,07/08)

ized (glass spheres) sediment samples, under controlled oscillatory pressure loading leading to soil liquefaction [16].

In this paper, we detail novel microfluidic experiments and their modeling. Mini-channels were fabricated and tested at URI for flow properties, in a newly designed aparatus (Fig. 1), with the goal of : (i) understanding and measuring the complex structure of dynamic pressure propagation in water filled channels (for reference) but, more importantly, in water-sediment mixtures; and (ii) to develop new macroscopic constitutive laws, relevant to the submarine landslide triggering problem. The second key component of this work was the CFD modeling of the new microfluidic experiments and earlier triaxial tests, in order to both gain additional physical insight into flow processes and use the model to perform a broader parametric study. The CFD simulations are performed with a model combining a pre-existing Lattice-Boltzmann model (LBM) and a "physics engine". The LBM, developed at TUB [21, 29, 6, 2], simulates fluid flows by solving a simplified Boltzmann equation (over a lattice) that can be shown, to the limit, to yield approximate solutions of Navier-Stokes equations. The sediment grains, represented by rigid spherical particles, interacting with each other and with the surrounding fluid, are modeled with the PE. Details of models are given later. Results of initial LBM simulations and of microfluidic experiments, f or academic and less academic test cases, are presented in the following, together with a summary of various methodologies.

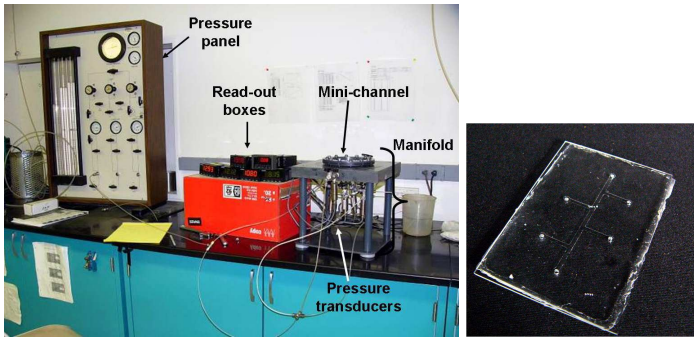

Figure 1: Experimental set-up (left). Example of mini-channel tested in the set-up, fabricated using soft lithography (right)

THE LATTICE BOLTZMANN METHOD

Many commercial CFD softwares (such as Fluent^{TM}) solve fluid dynamics using various forms of Navier-Stokes equations, derived from mass, momentum and energy conservation, assuming the fluid is s a continuum. In microfluidics applications, however, one is more interested in studying phenomena from a micro/meso-scale point-of-view. Hence, it appears more natural to consider the fluid as a group of particles, interacting with each other and with the surrounding medium, such as done with the LBM, or its ancestor the lattice-gas method, developed from the kinetic theory of gases. Hence, the LBM simulates compressible fluid behavior, but converges to an incompressible solution for low Mach numbers (i.e., when the fluid velocity is small compared to sound speed).

The primary variable of the Boltzmann equation is a particle distribution function $f(\boldsymbol{x}, t, \boldsymbol{v})$, which describes the (normalized) probability to find a particle with microscopic velocity $\boldsymbol{v}$ at point $\boldsymbol{x}$ (i.e., 3D positon vector) and time t. In the LBM, one defines a set of (b) discrete particle velocities $\boldsymbol{e}_i$, and a simplified collision operator $\boldsymbol{\Omega}$ (see, e.g., [26]). The resulting set of partial differential equations governing particle distributions and interacitons is given by,

$$\frac{\partial f_i}{\partial t} + \boldsymbol{e}_i \cdot \boldsymbol{\nabla} f_i = \Omega_i\{f_j\}, \quad i,j = 0,\ldots,b-1. \tag{1}$$

Here, the so-called D3Q19 model [24] is used to define relationships between particles over the lattice (3 dimensions, 19 velocities) with the following definition of constant microscopic velocities: $\{\boldsymbol{e}_i; i = 0,\ldots,18\} \equiv \{\{0,0,0\}, cycl\{\pm c,0,0\}, cycl\{0,\pm c,\pm c\}\}$, where c is a constant (Fig. 2).

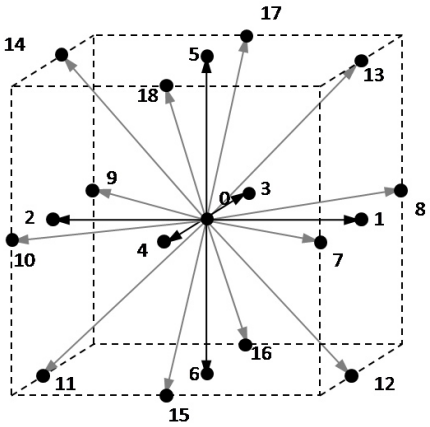

Figure 2: D3Q19 grid pattern used in LBM

Eqs. (1) are discretized by Finite Difference as,

$$f_i(t+\Delta t, \boldsymbol{x}+\boldsymbol{e}_i\Delta t) = f_i(t,\boldsymbol{x}) + \Omega_i, \; i = 0,\ldots,b-1, \tag{2}$$

where Δt is time step, $\Delta x = c\Delta t$ is grid spacing, and the so-called "Bhatnagar-Gross-Krook"-collision operator [3] (also known as single-relaxation-time collision operator) is given by,

$$\Omega_i = -\frac{\Delta t}{\tau}(f_i - f_i^{eq}). \tag{3}$$

with τ a microscopic relaxation time, measured in units of Δt, and f_i^{eq} the equilibrium distributions, which are usually taken as second-order polynomials of the moments, defined later following [24]. Eqs. (2) corresponds to a two-step procedure: (i) the distributions are modified by $\boldsymbol{\Omega}$ (collision step); and (ii) advected to the corresponding neighboring grid nodes (propagation step). Discrete moments are defined to compute the macroscopic fluid velocity $\boldsymbol{u}$ and hydrodynamic pressure p as,

$$\boldsymbol{u}(\boldsymbol{x},t) = \frac{1}{\rho(\boldsymbol{x},t)} \sum_i \boldsymbol{e}_i f_i(\boldsymbol{x},t) \tag{4}$$

$$p(\boldsymbol{x},t) = c_s^2\, \rho(\boldsymbol{x},t) = c_s^2 \sum_i f_i(\boldsymbol{x},t) \tag{5}$$

where $c_s^2 = c^2/3$ is the speed of sound. Using either a Chapman-Enskog expansion [13] or an asymptotic expansion based on the diffusive scaling [20], it can be shown that flow properties defined by these moments approximate those from weakly compressible Navier-Stokes equations, to the first-order in time and second-order in space, when assuming the following relationship between microscopic relaxation time and fluid kinematic viscosity $\nu : \tau = \Delta t\,(1 + 6\nu\Delta t/(\Delta x)^2)/2$.

For the simulations described below, we use a variant of the Multi-Relaxation Time model, which maps the distributions before collision to a set of well-defined moments, for which the non-conserved higher-order moments are relaxed, with different relaxation times, which are subject to optimization in terms of stabililty and accuracy. After the collision operator is applied, these moments are mapped back to the velocity space (i.e., the distributions) where the propagation step is computed. Details can be found in [5, 22, 6, 28].

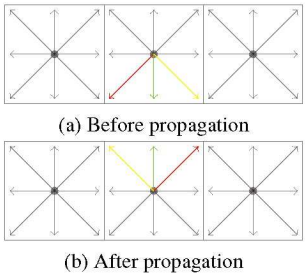

Figure 3: Simple bounce back scheme

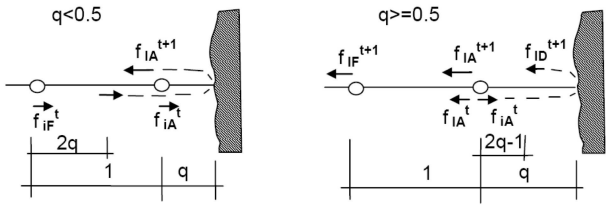

Figure 4: Second-order bounce-back scheme [15]

In the LBM, by nature, boundary conditions have to be directly specified on the distribution functions for the boundary nodes, which is quite different from macroscopic CFD methods. No-slip boundary conditions are modeled with a so-called bounce-back scheme, in which the particle distribution function "bounces" against the boundary, as shown in Fig.3, causing the mean momentum exchange to be equal to zero. This method can be extended to non-straight as well as moving boundaries, by using a second-order interpolation in the bounce-back scheme (Fig.4), identifying two different cases, depending on whether the distance q between the boundary and the node is : (i) $[0 - 0.5[\,|\boldsymbol{e}_i\Delta t|$; or (ii) $[0.5 - 1]\,|\boldsymbol{e}_i\Delta t|$. Formal interpolation schemes are given in Eq. (6),

$$f_{IA}^{t+1} = \quad (i) \quad (1-2q)f_{iF}^t + 2q\,f_{iA}^t - 2\rho\,w_i\frac{e_i u_w}{c_s^2} \qquad (ii) \quad \frac{2q-1}{2q}f_{IA}^t + \frac{1}{2q}\,f_{iA}^t - \rho\,w_i\frac{e_i u_w}{q c_s^2} \qquad (6)$$

where subscript I denotes the symmetrical distribution function, with $\boldsymbol{e}_I = -\boldsymbol{e}_i$. A good overview to the treatment of boundary conditions in the LBM can be found,e.g., in [17].

Forces on a rigid submerged body are evaluated in the LBM during the propagation, based on momentum transfer between fluid particles and the immerse body, resulting from collisions [23]. For a straight boundary, we have,

$$\Delta F = \frac{(\Delta x)^3}{\Delta t}(\boldsymbol{e}_i - \boldsymbol{u}_B)(f_i^t + f_I^{t+1}) \qquad (7)$$

with u_B the moving boundary velocity. This basic scheme can easily be extended to non-uniform grids (see, e.g., [4]).

The efficiency and accuracy of the LBM method to solve classic CFD problems has been demonstratde in many papers. A study of transient laminar flows, for instance, is presented in [14]. In addition, the method can be efficiently parallelized to benefit from massively parallel hardware [12].

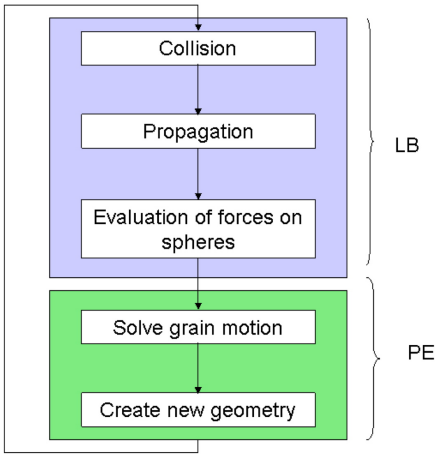

Figure 5: Flowchart for LBM-PE model coupling

RIGID BODY MODELING WITH LBM

The LBM model was applied to simulate the free fall of interacting rigid spheres of identical radius (aimed at representing sediment grains), in a fluid filled domain. To do so, the LBM model was coupled to a "physics engine" (PE) that model each sphere's motion and interactions, based on computed flow properties (Fig. 5). The PE is a particle-based method that simulates rigid body motions and interactions based on Newton's second law, applied to the spheres' center of mass. The PE handles the contact and collision responses between rigid bodies, depending of the bodies' relative velocity ($U_{rel} < 0$: separating contact; $U_{rel} = 0$: resting contact; $U_{rel} > 0$: colliding contact). The tolerance level of the contacts is set based on threshold values. Hydrodynamic forces applied to the rigid spheres are calculated during the collision part of the LBM. The spheres' impulse response is then calculated using a projected Gauss-Seidel solver. The initialization of new fluid nodes created as a result of the spheres'

displacement is done by performing local collision/propagation steps, on the newly created fluid nodes, until convergence of the fluid characteristics (pressure/higher order moment) is achieved. This approach has helped improving the forces' accuracy and reducing errors on both sphere drag force and velocity, as well as oscillations of various parameters during the simulations.

Practically, the PE consists in a library of C++ routines, developed at the University of Erlangen-Nurnberg (Germany) [11], that is coupled to the LBM model for computing spheres' interactions and resulting changes in flow properties, in the manner described above. The simulation of free falling spheres is split into two phases: (i) an initialization, in which each sphere is fixed to an initial position and the LBM model is run until convergence of flow properties to a steady state is achieved; (ii) each sphere is released to fall and interact with other spheres in the cylinder, under the action of gravity.

APPLICATIONS OF LBM-PE MODEL

Flow in a circular pipe

We simulate a gravity driven laminar flow, through a sloping circular pipe of radius R and angle α, by specifying volume forces : $dp/dx = \rho g \sin\alpha$ in the LBM. For laminar flows, Navier-Stokes equations yield the classical axisymmetric *Poiseuille flow* solution,

$$u = \frac{R^2 - r^2}{4\mu}\frac{dp}{dx} \tag{8}$$

with $\mu = \rho\,\nu$ the fluid dynamic viscosity.

The model is first run for a pipe of radius $R = 0.005$ m, slope angle $\alpha = 1°$, and length $L = 0.005$ m, with a fluid of density $\rho = 1,000$ kg/m^3 and kinematic viscosity $\nu = 0.0001$ m^2/s. The Reynolds number **Re** = $2\,u_{max}\,R/\nu = 1.07$ (with $u_{max} = 0.0107$ m/s for $r = 0$ from Eq. (8)) is well wihin the laminar regime. Results are calculated for a series of increasingly refined LBM grids sizes, $\Delta x = 5.10^{-4}$ to 1.10^{-4}, starting from a state of rest; in each case, time step is selected based on a CFL = 1 criterion. Periodic boundary conditions are specified at the inlet and outlet boundaries (i.e., fields on the inlet boundary are set equal to those on the outlet boundary at the previous time step) and a no-slip boundary condition is applied at the wall (second-order bounce-back scheme). Table 1 shows relative mean, maximum, and RMS errors of LBM results for the axial velocity u_{max} at the middle section of the pipe, compared to the theoretical value from Eq. (8), as a function of grid size. We see that numerical results converge to the analytic solution as grid size is reduced. A closer inspection would show that the convergence rate is $\propto (\Delta x)^2$, as expected from the selected LBM scheme.

The model is then run for higher slope angles, and thus Reynolds numbers, in order to verify that numerical errors remain acceptable. Mean, maximum, and RMS errors are similarly reported in Table 2, for the coarser grid size $\Delta x = 5.10^{-4}$. We see that numerical errors remain quite similar over a large range of Reynolds numbers within the laminar regime, **Re** $\simeq$ 1–21.

Δx	max. error	RMS error	mean error
5.10^{-4}	2.879	3.764	0.864
$2.5.10^{-4}$	1.452	1.483	0.237
$1.66.10^{-4}$	0.997	0.786	0.102
$1.25.10^{-4}$	0.754	0.556	0.063
1.10^{-4}	0.560	0.269	0.027

Table 1: Relative errors (%) of axial velocity u_{max}, compared to Eq. (8), as a function of LBM grid size for **Re** = 1.07.

α	**Re**	max. error	RMS error	mean error
1	1.07	0.560	0.270	0.027
10	10.65	0.523	0.258	0.026
20	20.97	0.523	0.256	0.026

Table 2: Relative errors (%) of axial velocity u_{max}, compared to Eq. (8), as a function of Reynolds number for $\Delta x = 5.10^{-4}$.

Single falling sphere in a fluid

Assuming a sphere of radius a and density ρ_s, falling in an unbounded Newtonian fluid of density ρ_w and viscosity μ, the balance of weight ($W = (4/3)\pi\,a^3\rho_s g$) buoyancy ($B = (4/3)\pi\,a^3\rho_w g$) and drag ($D = (1/2)\rho_w C_D\,\pi a^2 U^2$) forces ($W = B + D$) yields a terminal velocity of,

$$U = \left\{\frac{8g}{3C_D}a(s-1)\right\}^{1/2} \tag{9}$$

with $s = \rho_s/\rho_w$. Assuming **Re** $= 2aU/\nu) = \mathcal{O}(1)$ for laminar flows, Stokes solution yields the drag coefficent for the sphere : $C_D = 24/$**Re**.

Schiller and Naumann [25] extended the latter equation to higher **Re** values as, $C_D = 24(1 + 0.15\,$**Re**$^{0.687})/$**Re**. Moreover, for a finite width LBM domain, e.g., represented by a circular pipe of radius R, such as used in the above application, additional corrections must be made to C_D values. These were given in [10] as a perturbation expansion of $\lambda = a/R$, yielding,

$$C_{DW} = \frac{24}{\textbf{Re}}\left\{0.15\,\textbf{Re}^{0.687} + \frac{1 - 0.75857\lambda^5}{1 - 2.1050\lambda + 2.0865\lambda^3 - 1.7068\lambda^5 + 0.72603\lambda^6}\right\} \tag{10}$$

which predicts the drag force $D_W = (1/2)\rho_w C_{DW}\,\pi a^2 U^2$ with a 95% accuracy, for $\lambda < 0.6$ and **Re** < 50.

We run the LBM model for : $R = 0.05$ m, $a = 0.005$ m, $\rho_s = 2,000$ kg/m^3, $\nu = 0.001$ m^2/s and $\rho_w = 1,000$ kg/m^3; length $L = 0.2$ m was selected in order for the sphere to reach steady state before impacting the cylinder's bottom. No-slip conditions are specified on the lateral boundary as well as on the top and bottom sides of the cylinder, as recommended in [23]. A velocity continuity boundary condition is specified on the rigid sphere's boundary (modified second-order bounce-back scheme

Δx	Error on C_{DW}	Error on U
0.0025	0.07	16.69
0.0017	0.08	9.16
0.0013	0.15	7.90
0.001	0.06	8.88

Table 3: Relative error (%) of computed drag coefficient C_{DW} and fall velocity of the sphere U, as compared to theory (Eqs. (9) and (10)) for different grid sizes and **Re**=0.41.

ρ_s	**Re**	Error on C_{DW}	Error on U
2,000	0.41	0.06	8.88
4,000	1.15	0.02	10.69
6,000	1.83	0.01	11.04
8,000	2.47	0.06	10.66
10,000	3.09	0.29	9.84

Table 4: Same errors as in Table 3, for different **Re** values, with $\Delta x = 0.001$.

for moving boundaries, defined in [23]). We first performed computations in a series of increasingly refined LBM grids, with size $\Delta x = 0.0025$ to 0.001, starting from a state of rest. As before, time step is selected based on a CFL = 1 criterion. Table 3 shows numerical errors for C_{DW} and U as compared to Eqs. (9) and (10), for a low **Re**=0.41, as a function of mesh size. We see a reasonable convergence of numerical results towards the expected values. We then use $\Delta x = 0.001$ to compute the drag coefficient and fall velocity as a function of **Re** (changed by varying the sphere density). Table 4 shows a good accuracy for all selected cases.

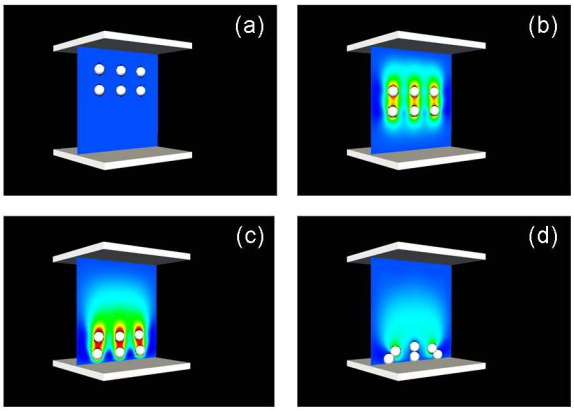

Figure 6: Simulation of 6 falling spheres (color scale indicates velocity magnitude) ; (a)-(d) shows results for increasing time.

Multiple-spheres test-cases

Having validated LBM simulations for both a Poiseuille flow and for one single falling/settling sphere, other cases were performed for multiple interacting falling spheres, for which no theoretical solution exists. Fig. 6 thus shows 4 stages of flow

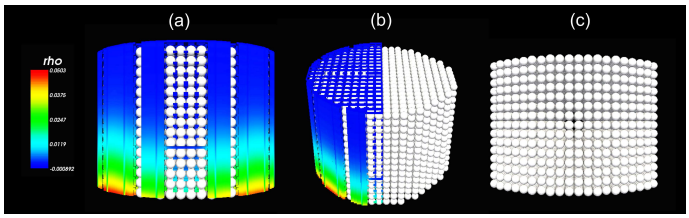

Figure 7: LBM-PE simulations with 4,500 spheres in a cylindrical domain, for a specified inlet velocity achieving **Re** = 0.1; in (a)-(b), color reflect a pressure scale

and interactions of 6 falling spheres. Steady state is reached in Fig. 6b and, in Fig. 6c, the 3 leading spheres are approaching the bottom and slow down. Hence, flow velocities increase ahead of the 3 following spheres. In Fig. 6d, spheres impact the cylinder bottom, rebound, and roll over each other.

Perspectives

More complex applications, which are still ongoing, will ultimately involve the computation of unsteady flows in a circular (or rectangular) domain filled with a large number N (typically 10,000) of interacting spheres of varying radii a_i, achieving a specified porosity n, e.g., representing a porous medium in a mini-channel. For a cylindrical domain (R, L), for instance, we find,

$$n = 1 - \frac{4}{3R^2L}\sum_{i=1}^{N} a_i^3 \tag{11}$$

Similar to the work in [32], we are first testing cases of a steady flow through a sphere-filled pipe (e.g., Fig. 7), to verify the standard Darcy law is retrieved for low porosity n. We will then test cases with cyclic pressure loading at the pipe extremities and/or harmonic horizontal acceleration specified as a volume force. Such cases will yield soil liquefaction under some specific loading.

MICROFLUIDICS EXPERIMENTS

Experiments were performed in custom fabricated mini-channels (Fig. 1) filled with water, or with a mixture of water and idealized sediment made of standardized glass beads of 10-50μm in diameter, to both provide data for LBM-PE model validation and gain physical insight into the pore pressure response of soils, due to dynamic seismic-like loading. Two different types of experiments were designed and performed, for which pressure variation was measured at several gates (side channels) along the main channel, using pressure transducers connected to a manifold (Fig. 1) : (a) steady state flows were created by specifying a constant pressure gradient between both extremitites of the mini-channel; and (b) dynamic (essentially cyclic) pressure pulses were generated in the mini-channel using a pump.

We only tested one channel geometry so far, but we are planning in future work to vary properties of the channel (cross-section/length/branches), together with the frequency and amplitude of the pressure variation, in order to investigate effects of

these on measurements, in relation to pore pressure generation in soils.

In all experiments, we first use pure water and estimate effects of the channel itself on fluid flow, essentially through energy dissipation; this yields hydrodynamic characteristics of the channel (e.g., friciton coefficient). We then repeat experiments using the mixture of water and glass beads and estimate the hydrodynamic properties of glass beads by removing the known channel effects. Cyclic test results will be processed this way and we will then attempt to correlate these to triaxial test results [16] and CFD simulations of both with the LBM-PE model.

Mini-channel and its equipment

Considerable efforts in miniaturization since the 1980s led to the development of Micro Electro Mechanical Systems (MEMS), such as mini- and micro-channels, and to their increasing use in chemichal and biomedical applications. Here, we built mini-channels by soft-lithography, which allows for a quick fabrication of rectangular mini-channels, using the properties of polymerization of polydimethylsiloxane (PDMS).

The mini-channel shown in Fig. 1, used in experiments reported here, is $L = 50$ mm long, 1 mm wide, and 0.2 mm deep. Four branches, spaced 10 mm apart, allow for pressure measurements using transducers connected to 4 gates; 2 additional gates are located at the entrance and exit of the main channel. These six gates are connected to pressure transducers via a custom made manifold (Fig. 1) The transducers are Honywell type stainless steel strain gauges (non-linearity of +/- 0.1% of the full scale, pressure range : 0–200 psi), and Omega DP25-S strain gauge panel meters are used to digitize the pressure (Fig. 1); these are connected to a control unit recording measurements at a specified sampling frequency (typically 12 Hz). A pressure panel (Fig. 1) is used to specify a constant or cyclic pressure at the channel inlet.

Experiments

Eq. (8) gives the axial flow velocity $u(r)$, in a circular cylinder of radius R, due to a specified pressure gradient, for steady laminar flows with low **Re** (Poiseuille flow). The latter is typical in microfluidics applications dominated by viscosity. Eq. (8) can still be used as a reference for non-circular channels by introducing the hydraulic diameter, $D_h = 4A/P$, where A is the channel cross-sectional area and P its perimeter. We further define: **Re** $= U\,D_h/\nu$, with $U = Q/A$ the mean flow velocity, where Q denotes flow rate. With these definitions, Eq. (8) yields,

$$u = u_{max}\left(1 - \frac{4r^2}{D_h^2}\right) \qquad \text{with} \qquad u_{max} = \frac{\partial p}{\partial x}\,\frac{D_h^2}{16\mu} \quad (12)$$

and $U = u_{max}/2$ for a circular cross section. For Fig. 1's channel : $A = 0.2$ mm^2, $P = 2.4$ mm and $D_h = 0.333$ mm.

In fluid flows through narrow pipes, changes in pressure take place along the length of the pipe, due to both continuous and discrete frictional losses. The former are due to viscous shear stress along the pipe boundary, as in Eq. (12), while the latter are additional energy losses due to abrupt changes in the pipe geometry, such as branching-out/inlet/outlet. Hence, the specified pressure gradient, $\partial p/\partial x = (p_1 - p_2)/L$, must overcome all such pressure drops (i.e., head losses) due to energy losses, with p_1 the pressure at the inlet and p_2 at the outlet. If the mini-channel cross-section remains constant, for a constant flow rate, there is no change in mean flow velocity along the pipe. Bernouilli equation can then be used to relate the total energy loss along the channel to the specified pressure difference, $\Delta p = p_1 - p_2$. Assuming a horizontal channel, we find,

$$\Delta p = \frac{1}{2}\rho U^2\left(\frac{C_f}{D_h} + \sum_i K_i\right) \quad (13)$$

with C_f the average (continuous) skin friction coefficient and K_i the i-th discrete head loss coefficient.

In mini-channel experiments with steady flows (Fig. 1), Eq. (13) can be applied between each pair of pressure gates. Thus, using measured pressures, values of C_f and K_i are first calculated as a function of U (or more specifically as a funcion of **Re**). Results are first calculated for pure water and then for the water-beads mixture. The channel frictional properties can thus be removed to estimate those of the idealized saturated porous medium modeled by the glass beads, under various types of flows.

According to Darcy's law, in a porous medium of low permeability k (i.e., clays, silts), the small flow velocity is proportional to the pressure gradient: $\Delta p = (\rho g L/k)\,U$; this applies when **Re** $<$ 1,000 or so. For larger permeability and **Re** values, according to Vorchheimer equation, a quadratic term appears : $\Delta p = (\rho g L/k)\,U + \beta U^2$; this applies when **Re** $>$ 10,000 or so. Eq. (10) is consistent with Darcy's law prediction, since for small **Re** : $C_D \simeq C_f \propto 1/$**Re** $\propto 1/U$; hence, Eq. (13) yields $\Delta p \propto U$ for the continuous friction term. By contrast, for large **Re**, the drag coefficient of a small rigid sphere becomes constant in the turbulent regime and Eq. (13) yields $\Delta p \propto U^2$ for the continuous friction term, which is consistent with Vorchheimer equation.

Fig. 8 shows the pressure p measured at gates G1-G5 as a function of mean flow speed U, in the mini-channel of Fig. 1 filled

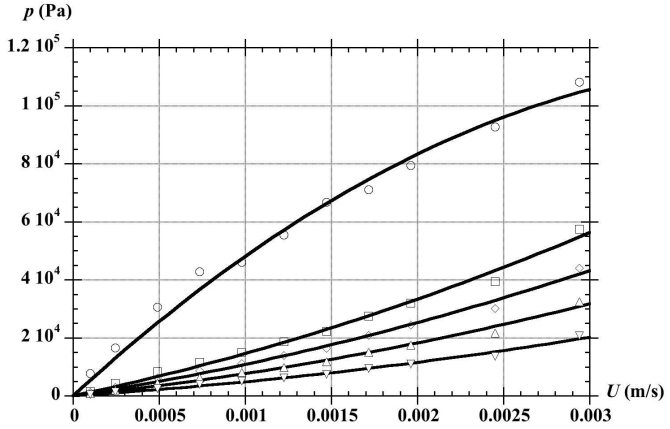

Figure 8: Pressure measured as a function of mean flow speed, in Fig. 1's channel, filled with a water-bead mixture, at gate : G1 (inlet) ($\circ$); G2 ($\Box$); G3 ($\Diamond$); G4 ($\triangle$); G5 ($\bigtriangledown$). Solid lines denote quadratic curve fits forced to (0,0); $p = 0$ (atmosph.) at gate G6.

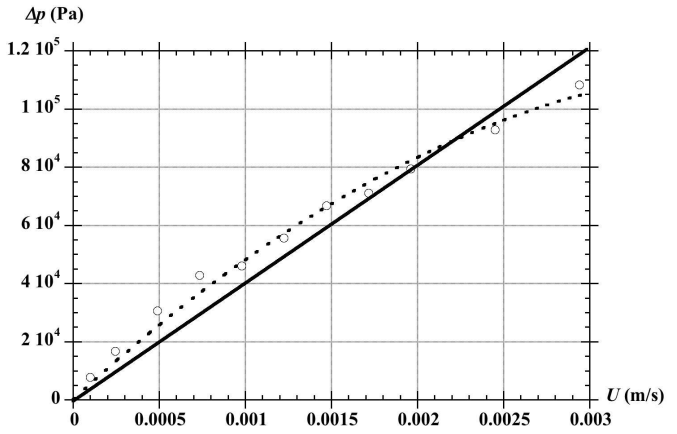

Figure 9: Pressure drop between inlet and outlet, as a function of flow speed, in Fig. 1's channel filled with a water-bead mixture : measurements (∘); linear (——) and quadratic (- - - -) fits.

with a water-beads mixture. G1 denotes the inlet, and pressure at the outlet G6 is atmospheric, $p_6 = 0$. Hence, in this configuration, $\Delta p = p_1 - p_6$. We see, pressure varies linearly for low U (< 0.001 m/s) and then becomes quadratic. Specificaly, Fig. 9 plots Δp as a function of U and shows both linear and quadratic fits, representative of Darcy's and Vorchheimer's laws, respectively. With the former, we find $k = 1.22\,10^{-5}$ m/s ($R^2 = 0.984$), and with the latter $k = 0.899\,10^{-5}$ m/s ($R^2 = 0.987$). For $U = 0.003$ m/s, the maximum observed value of the mean velocity, we have **Re** = 1, indicating laminar creeping flows in all cases.

Similar experiments, run with the mini-channel filled only with water showed, as expected, much larger velocities, varying between $U = 0$ and 2 m/s for the same pressure gradients as in Fig. 8. Eq. (13) was applied to those measurements and frictional characteristics of the mini-channel, C_{fw} and $K_i; i = 1, \ldots, 6$, were calculated. For the continuous friction coefficient we found, in particular, $C_{fw} = 2078\,\mathbf{Re}^{-1.61}$ (with $R^2 \simeq 1$). A similar analysis was repeated for the results of Fig. 8 obtained for the mini-channel filled with the water-bead mixture. We thus found, $C_f = C_{fw} + C_{fb} = 30,283\,\mathbf{Re}^{-1.24}$ (with $R^2 = 0.999$), yielding the continuous friction coeficient due only to the water-bead medium as, $C_{fb} = 28,855\,\mathbf{Re}^{-1.18}$, which is close to the theoretical value expected from Darcy's law. Additionally, the discontinuous K_i coefficients for the water-bead filled channel were obtained (not shown). These results, together with various forms of Eq. (13), make it possible to predict the pressure at gates G1-G6, without running experiments, including various contributions to the pressure drop, Fig. 10, for instance shows such a prediction for $U = 0.00245$ m/s.

CONCLUSIONS

Although computations described in the perspective section are sill ongoing and no comparison with microfluidics results were done so far, based on prelminary results, we believe our LBM-PE approach is more general, consistent, and accurate than earlier proposed methods, and will yield a numerical tool able to

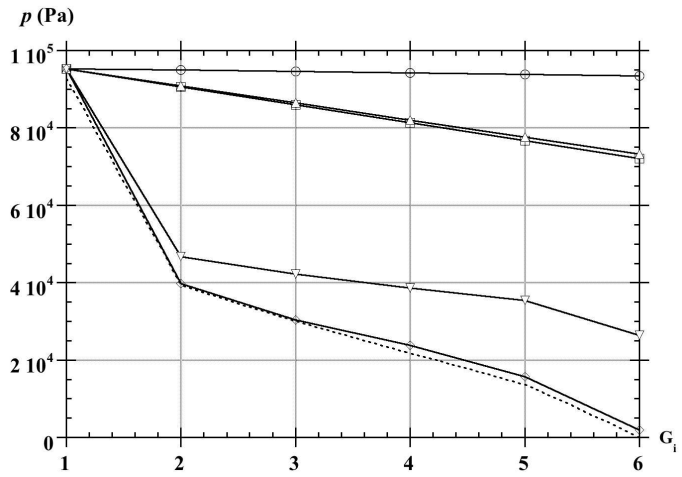

Figure 10: Pressure at gages G1-G6, for $U = 0.00245$ m/s, in Fig. 1's channel filled with water-bead mixture : predicted continuous losses in channel (C_{fw}) (∘); predicted continuous losses due to beads (C_{fb}) (△); total predicted continuous losses (C_f) (□); predicted discrete losses due to branching (K_i) (▽); total predicted losses (◇); total measured losses (- - - -).

investigate the micro-mechanical behavior of soilds under complex seismically induced harmonic pore pressures and horizontal accelerations.

Initial experiments performed in mini-channels filled with an idealized sediment, for steady flows, led to promising results showing the expected fluid behaviors at the of the micro-mechanical level. Experiments with cyclic pressure loading are ongoing and will be similarly analyzed in order to relate macroscopic measured parameters, such as pressure drop, to the micro-mechanical properties of the medium. These experiments will both help gaining additional physical insight into pore-pressure build-up and serve as a data set for validating the LBM-PE model, which in turn wil be use to perform broader parametric studies.

Ultimately, all these results will contribute to developing new macroscopic constitutive laws for predicting underwater slide triggering.

ACKNOWLEDGEMENTS

This research was supported by the NSF-PIRE program at URI and the TUB. The author would like to thank Klaus Iglberger (University of Nurnberg-Erlangen).

REFERENCE

[1] Abadie, S., Morichon, D., Grilli, S.T. and Glockner, S. (2008) "VOF/Navier-Stokes numerical modeling of surface waves generated by subaerial landslides," *La Houille Blanche*, **1** (Feb. 2008), 21-26.

[2] Ahrenholz, B., Tolke, J. and Krafczyk, M. (2006) "Lattice-Boltzmann simulations in reconstructed parametrized porous media," *Intl. J. Comp. Fluid Dyn.*, **20**(6), 369-377.

[3] Bhatnagar, P.L., E.P. Gross and M. Krook (1954) "A Model for Collision Processes in Gases," *Phys. Rev.*, **94**, 511-.

[4] Crouse, B., E. Rank, M. Krafczyk and J. Tölke (2002) "A LB-based approach for adaptive flow simulations," *J. Modern Phys B*, **17**, 109-112.

[5] d'Humières, D. (1992) "Generalized lattice-Boltzmann equations," *Rarefied Gas Dynamics: Theory and Simulations* (Prog. Astronaut. Aeronaut., B. D. Shizgal and D. P. Weave, eds.), AIAA, Washington DC, Vol. **159**, 450–458.

[6] d'Humières, D., Ginzburg, I., Krafczyk, M., Lallemand, P., and Luo, L. (2002) "Multiple-relaxation-time lattice Boltzmann models in three dimensions," *Phil. Trans. R. Soc. Lond.*, **A360**, 437-451.

[7] Drouin Y. (2006) *Study of soil liquefaction and its effects on tsunamogenics landslides.* Senior Thesis Report, Ecole Centrale de Nantes/University of Rhode Island. 69 pps.

[8] Enet F. and Grilli S.T. (2005) "Tsunami Landslide Generation: Modelling and Experiments," *In Proc. 5th Intl. on Ocean Wave Measurement and Analysis* (Madrid, Spain, July 2005), IAHR Publ., paper 88, 10 pps.

[9] Enet, F. and Grilli, S.T. (2007) "Experimental Study of Tsunami Generation by Three-dimensional Rigid Underwater Landslides," *J. Waterway Port Coast. and Oc. Engng.*, 133(**6**), 442-454.

[10] Fayon, A., Happel, J. (1960) "Effect of a cylindrical boundary on fixed rigid sphere in a moving fluid," *AIChE J.*, **6**(1), 55-58.

[11] Freudiger, S., J. Hegewald and M. Krafczyk (2008) "Simulation of moving particles in 3D with the Lattice Boltzmann method," *Comput. Math. with Appl.*, **55**, 14611468.

[12] Freudiger, S., J. Hegewald and M. Krafczyk (2008) "A parallelization concept for a multi-physics lattice Boltzmann prototype based on hierarchical grids," *Intl. J. Comp. Fluid Dyn.* (in press).

[13] Frisch, U., D. d'Humières, B. Hasslacher, P. Lallemand, Y. Pomeau and J.-P. Rivet (1987) "Lattice Gas Hydrodynamics in Two and Three Dimensions," *J. Complex Syst.*, **1**, 75–136.

[14] Geller, S., M. Krafczyk, J. Tölke, S. Turek and J. Hron (2006) "Benchmark computations based on Lattice-Boltzmann, Finite Element and Finite volume Methods for laminar Flows," *Comp. and Fluids*, **35**, 888–897.

[15] Geller, S., J. Tölke and M. Krafczyk (2007) *Lattice-Boltzmann Method on quadtree type grids for Fluid-Structure-Interaction*, TU Braunschweig.

[16] Gemme, D.A. (2008) *Effect of Particle Size on Dynamic Pore Pressure Buildup in Soils*. Master's Thesis, Dept. of Ocean Engng., Univ. of Rhode Island, 88 pps.

[17] Ginzburg, I. and D. d'Humières (2003) "Multireflection boundary conditions for lattice Boltzmann models," *Phys. Rev.*, **68**, 606-614.

[18] Grilli, S.T., Ioualalen, M, Asavanant, J., Shi, F., Kirby, J. and Watts, P. (2007) "Source Constraints and Model Simulation of the December 26, 2004 Indian Ocean Tsunami," *J. Waterway Port Coast. and Oc. Engng.*, 133(**6**), 414-428.

[19] Grilli, S.T. and Watts, P. (2005) "Tsunami generation by submarine mass failure Part I : Modeling, experimental validation, and sensitivity analysis," *J. Waterway Port Coast. and Oc. Engng.*, 131(**6**), 283-297.

[20] Junk, M., A. Klar and L.-S. Luo (2005) "Asymptotic analysis of the lattice Boltzmann equation," *J. Comp. Phys.*, **210**(2), 676–704.

[21] Krafczyk, M., Lehmann, P., Philippova, O., Hnel, D. and Lantermann, U. (2000) "Lattice Boltzmann Simulations of complex Multi-Phase Flows,Multifield Problems: State of the art", Hrsg.: A.-M.-Sndig et al., *Springer Verlag*, 50-57.

[22] Lallemand, P. and L.-S. Luo (2000) "Theory of the lattice Boltzmann method: Dispersion, dissipation, isotropy, Galilean invariance, and stability," *Phys. Rev.*, **61**(6), 6546–6562.

[23] Nguyen, N.Q., Ladd, A.J.C. (2004) "Sedimentation of hard-sphere suspensions at low Reynolds number," *J. Fluid Mech*, **535**, 73-104.

[24] Qian, Y. H. , D. d'Humières and P. Lallemand (1992) "Lattice BGK models for Navier-Stokes equation," *Europhys. Letters*, **17**(6), 479–484.

[25] Schiller, L., Naumann, A.Z. (1933) "Über die grundlegenden Berechnungen bei der Schwerkraftaufbereitung," *Zeitschrift Des Vereines Deutsc. Ing.*, **77(12)**, 318-320.

[26] Succi, S. (2001) *The Lattice Boltzmann Equation for Fluid Dynamics and Beyond*. Oxford University Press.

[27] Tappin, D.R., Watts, P. and Grilli, S.T. (2008) "The Papua New Guinea tsunami of 1998: anatomy of a catastrophic event," *Natural Haz. and Earth Syst. Sc.*, **8**, 243-266.

[28] Tölke, J., S. Freudiger and M. Krafczyk (2006) "An adaptive scheme for LBE multiphase flow simulations on hierarchical grids," *Comp. and Fluids*, **35**, 820-830.

[29] Tölke, J., Krafczyk, M., Schulz, M. and Rank, E. (2002) "Lattice Boltzmann simulations of binary flow through porous media," *Phil. Trans. R. Soc. Lond.*, **A360**, 535-545.

[30] Watts, P., Grilli, S.T., Kirby, J. T., Fryer, G. J. and Tappin, D. R. (2003) "Landslide tsunami case studies using a Boussinesq model and a fully nonlinear tsunami generation model," *Natural Haz. and Earth Syst. Sc.*, **3**, 391-402.

[31] Watts, P., Grilli, S.T., Tappin D., and Fryer, G.J. (2005) "Tsunami generation by submarine mass failure Part II : Predictive Equations and case studies," *J. Waterway Port Coast. and Oc. Engng.*, 131(**6**), 298-310.

[32] Zeghal, M. and El Shamy, U. (2004) "Dynamic response and liquefaction of saturated granular soils: a micromechanical approach," *Cyclic Behaviour of Soils and Liquefaction Phenomena*. Taylor & Francis Group, London.